Ocean Sci. Discuss., 6, 129–151, 2009
www.ocean-sci-discuss.net/6/129/2009/

Ocean Science Discussions

Papers published in *Ocean Science Discussions* are under open-access review for the journal *Ocean Science*

The multifractal structure of satellite sea surface temperature maps can be used to obtain global maps of streamlines

A. Turiel[1], V. Nieves[1], E. Garcia-Ladona[1], J. Font[1], M.-H. Rio[2], and G. Larnicol[2]

[1]Institut de Ciències del Mar, CSIC, Barcelona, Spain
[2]CLS – Space Oceanography Division, Toulouse, France

Received: 18 November 2008 – Accepted: 8 December 2008 – Published: 22 January 2009

Correspondence to: A. Turiel (turiel@cmima.csic.es)

Published by Copernicus Publications on behalf of the European Geosciences Union.

Abstract

Nowadays Earth observation satellites provide information about many relevant variables of the ocean-climate system, such as temperature, moisture, aerosols, etc. However, to retrieve the velocity field, which is the most relevant dynamical variable, is still a technological challenge, specially in the case of oceans. New processing techniques, emerged from the theory of turbulent flows, have come to assist us in this task. In this paper, we show that multifractal techniques applied to new Sea Surface Temperature satellite products opens the way to build maps of ocean currents with unprecedented accuracy. With the application of singularity analysis, we show that global ocean circulation patterns can be retrieved in a daily basis. We compare these results with high-quality altimetry-derived geostrophic velocities, finding a quite good correspondence of the observed patterns both qualitatively and quantitatively. The implications of this findings from the perspective both of theory and of operational applications are discussed.

1 Introduction

Earth observation satellites provide an excellent platform for continuously monitoring the climatic evolution of our planet. Present remote sensors provide, on a rutinary basis and at global scales, a wide set of measured variables such as Sea Surface Temperature (SST), water vapor content in atmosphere, ocean surface chlorophyll concentration, aerosol concentration in air and a long etc. Atmospheric and ocean studies have largely been benefited from it, although the characterization of ocean dynamics by means of satellite observations is however more elusive than that of atmosphere. First, because due to the highest optical extinction of ocean water, our satellite-based knowledge about the ocean is limited to a narrow layer close to surface, of a depth going from millimeters to a few meters. Second, because despite some recent developments in Doppler radar shift (Chapron et al., 2005; Johannessen et al., 2005), to

OSD

6, 129–151, 2009

directly obtain a crucial dynamic variable as the ocean velocity field from satellites is still a challenging task.

Velocities can be retrieved through the Sea Surface Height (SSH) measurements from radar altimetry. The SSH field is linked to the pressure field and then the geostrophic approximation may be used to derive the velocity field. As a result quasi-synoptic maps can be build through the interpolation of several altimeters (Traon et al., 1998) and have been used to study the ocean variability at relatively large scales (Wunsch and Stammer, 1998). Sampling limitations as well as the necessity to combine the signals of several altimeters limit the spatial and time resolutions and prevent altimetry maps to resolve part of the relevant oceanic processes (Pascual et al., 2006).

An alternative strategy to evaluate ocean surface velocities from satellite data is to process sequences of images of SST (Bowen et al., 2002) or other scalars (Crocker et al., 2007). These techniques are based on tracking ocean structures which have been generated by the flow and are still being dragged (advected) by it. This strategy leads to useful velocity fields, although the spatial and temporal resolutions are relatively limited due to processing needs, and sometimes the field is not well resolved. However, satellite images of scalar variables can still be further exploited to gain insight about the dynamics, taking advantage of the turbulent structure of ocean flows.

When turbulence develops in a flow, a very complicated structure raises. In a turbulent flow, intermittency is revealed as dramatic changes of velocity and other properties as one moves across the fluid domain. As a consequence, shear is dominant over many areas; scalar parcels dragged by two different filaments rapidly separate from each other and so the flow is continuously creating new singularity fronts. By singularity we understand that the value of the local singularity exponent (a measure of the function regularity (Daubechies, 1992; Turiel and Parga, 2000)) decreases, what means that the function becomes more irregular. Therefore, in a scalar submitted to turbulence singularities are created in a statistically steady rate. Hence, each time a singularity is observed in a scalar it would probably indicate the presence of a strong velocity gradient (Kraichnan, 1968; Lapeyre et al., 2001). In fact, in previous works

OSD
6, 129–151, 2009

(Turiel et al., 2005b; Isern-Fontanet et al., 2007; Turiel et al., 2008a) some authors have argued that extracting singularities from satellite images as SST maps serves to delineate flow streamlines. Expressed in other words, singularity exponents are advected by the flow, what is an appropriate assumption as far as the stirring by the horizontal advection is the main singularity-inducing effect. This hypothesis is supported by the facts that at the mesoscale ocean flows are practically bi-dimensional and dominated by geostrophic balance and both SST and Chlorophyll images exhibit a common turbulent signature (Nieves et al., 2007).

In this paper, we will prove for the first time that singularity exponents derived from microwave SST maps serve to trace streamlines of surface currents, and at the same time we will validate a new generation of altimeter products. In Sect. 2 we will present the data to be used in this study. Then, in Sect. 3 the concept of singularity exponent field of a scalar map is introduced and discussed, and some examples are shown. We thus proceed to Sect. 4, where the streamlines derived from singularity analysis of SST maps are compared with altimetry-derived geostrophic currents. Finally, the conclusions are presented in Sect. 5. Technical details are presented in the Appendices.

2 Description of the data

Our main source of data for this study are Optimally Interpolated (OI) SST images from Microwave (MW) Radiometer SSTs. Microwave OI SST data are produced by Remote Sensing Systems and sponsored by National Oceanographic Partnership Program (NOPP), the NASA Earth Science Physical Oceanography Program, and the NASA REASoN DISCOVER Project. Data are available through the following web site: http://www.remss.com.

As SST images contain irregularly spaced data (in time and space) due to orbital gaps or environmental conditions, an interpolation of the data onto a regularly sampled grid is needed to make up for this missing data. MW SST products accurately resolve some features that could be missed due to data gaps or weather condition.

OSD
6, 129–151, 2009

This is possible by blending TMI and AMSR-E SSTs, providing nearly complete global coverage each day. Near real time OI SST products are created daily, even if no new observations exist. However, the product is 0.25×0.25 degree gridded, which is a coarse resolution in comparison with the standard infrared SSTs one. Processing details can be found in Reynolds and Smith (1994) and at the following website: http://www.ssmi.com/sst/microwave_oi_sst_browse.html.

The second source of data for this study are geostrophic surface currents computed at CLS in the framework of the SURCOUF project (Larnicol et al., 2006). Two types of currents maps are produced by SURCOUF. First, real time global maps of surface currents, which are produced daily on a 1/3° Mercator grid. Second, a reanalysis of these currents exists for the period June 1999–January 2006. In this study, the SURCOUF daily delayed-time maps of absolute geostrophic surface currents are used for the period September 2002 to August 2003. This period is particularly interesting since four altimetric satellites (Jason-1, ERS2/ENVISAT, TOPEX interleaved, GFO) were working together, allowing a much improved description of the ocean mesoscale (Pascual et al., 2006).

SURCOUF currents are based on the use of the altimetric data distributed by AVISO (http://www.aviso.oceanobs.com) and processed through the following steps: First, the usual geophysical corrections were applied to the altimetric heights from the four satellites (apart from GFO, for which specific corrections were applied (Traon et al., 2003)) and Sea Level Anomalies were computed subtracting from the instantaneous altimetric heights a 7 year (1993–1999) mean profile. Specific processing was applied to TP interleaved and GFO to achieve consistency with the Jason-1 and ERS2-ENVISAT missions (Traon et al., 2003; Traon and Dibarboure, 2004). Then the along-track anomalies from the four different missions were mapped into a global 1/3° resolution Mercator grid using a procedure described in Traon et al. (2003) and the observed Combined Mean Dynamic Topography RIO05 (Rio et al., 2005) was added to the SLA maps in order to retrieve daily maps of absolute ocean topography. The surface velocity currents were finally computed from the absolute topography maps using the geostrophic assump-

OSD
6, 129–151, 2009

tion. In the equatorial band the quasi geostrophic approximation is applied (Lagerloef et al., 1999).

3 Characterization of streamlines by singularity exponents

The first step in our work is to design stable, high-performance tools to perform singularity analysis on real images, capable to assign an accurate value of singularity exponent at each point. The singularity exponent of a scalar at a given point is a scale-invariant, dimensionless measure of the degree of regularity or irregularity of the function at that point (see Isern-Fontanet et al., 2007, and Turiel et al., 2008a, for a full discussion of the concept). As furnished by the acquisition devices, images (properly speaking, 2-D maps of a given variable) do not vary continuously on space but are sampled on a discrete grid, and are also affected by several sources of error, noise and acquisition problems. Hence, singularity analysis must implement appropriate filtering and interpolation schemes (Daubechies, 1992; Arneodo et al., 1995).

In this paper, we have used the same strategy developed in Turiel and Parga (2000), which has been shown to attain good spatial and value accuracy in the determination of singularity exponents in many contexts and in particular for the processing of satellite imagery (Turiel et al., 2005a,b; Isern-Fontanet et al., 2007; Nieves et al., 2007; Turiel et al., 2008a). We will denote the scalar under study by $\theta(\boldsymbol{x})$ (where θ can be SST, chlorophyll concentration, etc, and $\boldsymbol{x}$ denotes the point in the image plane). At each location $\boldsymbol{x}$ the singularity exponent $h(\boldsymbol{x})$ can be obtained by processing the wavelet projections (Daubechies, 1992; Mallat, 1999) of the modulus of the gradient of θ, that we denote by $T_\Psi[|\nabla\theta|](\boldsymbol{x}, r)$ and are defined as follows:

$$T_\Psi[|\nabla\theta|](\boldsymbol{x}, r) \equiv \int d\boldsymbol{x}' \, |\nabla\theta|(\boldsymbol{x}') \frac{1}{r^2} \Psi\left(\frac{\boldsymbol{x} - \boldsymbol{x}'}{r}\right) \quad (1)$$

As shown in previous works (Turiel et al., 2005b; Isern-Fontanet et al., 2007; Nieves et al., 2007) the wavelet projection of gradients of SST and other scalars depend on

OSD
6, 129–151, 2009

the scale resolution parameter r as a power-law, characterized by the local singularity exponent $h(\boldsymbol{x})$ in the way:

$$T_\Psi[|\nabla\theta|](\boldsymbol{x}, r) = \alpha(\boldsymbol{x}) r^{h(\boldsymbol{x})} + o\left(r^{h(\boldsymbol{x})}\right) \quad (2)$$

where the expression $o\left(r^{h(\boldsymbol{x})}\right)$ means a term which is negligible compared to $r^{h(\boldsymbol{x})}$ when $r^{h(\boldsymbol{x})}$ goes to zero. Scalars submitted to turbulence present local power-law scaling at each one of its points as the one expressed by Eq. (2). This is connected to the Microcanonical Multifractal Formalism (Turiel et al., 2008b): Eq. (2) implies that θ is multifractal (i.e. a composite of multiple fractal interfaces) and at the same time allows to explicitly separate each fractal interface from a given signal $\theta(\boldsymbol{x})$ (in contrast with classical approaches, which only allow a statistical characterization of the fractal components (Frisch, 1995)).

In Fig. 1 we show an example of singularity analysis on a global map of Microwave (MW) Sea Surface Temperature (SST); for details on the obtaining of singularity exponents see Appendix A. Many hydrographic features of global and regional ocean circulation become evident in the singularity map. Main boundary currents, such as the Gulf Stream, the Kuroshio, the Agulhas retroflection current or the Falkland current, as well as the diverse filaments of the Antartic Circumpolar Current, which can be vaguely distinguished in SST maps, become clear and distinct in the singularity map, in addition with other emerging filaments, eddies and currents that were hidden in the SST maps. Notice that even accepting that singularity exponents serve to delineate the streamlines of the flow, they do not offer information about the velocity modulus or sense, only about its direction. However, this information is already very useful to understand ocean circulation. In the following we will discuss on the validation of singularity streamlines.

OSD
6, 129–151, 2009

4 Comparison with altimetry

Although the singularity maps derived from MW SST that we have presented are appealing and seem to be highly correlated with the geometrical arrangement of currents in oceans, we need to confirm their validity as current tracers. Hence, we need independent measurements to contrast the similitudes and to quantify the degree of closeness between ocean currents and the filaments shown in singularity maps. However, this is precisely the question: we have no synoptic maps of ocean currents. Nevertheless, for a more than a year between 2002 and 2003 high-quality daily maps of geostrophic currents derived from the combination of four satellite altimeters are available (Pascual et al., 2006). Hence, we have used these data, produced by CLS, as a reference in the present study.

In Fig. 2 we show a couple of examples of the comparison of singularity maps derived from MW SST and high-quality altimeter maps, for two different regions. The visual assessment indicates that singularities align quite well with altimeter-derived geostrophic currents.

However, a simple visual comparison does not allow to quantify the degree of closeness between altimeter-derived currents and singularity lines. Hence, we have estimated the advective and the material derivatives of the singularity exponents $h(\boldsymbol{x}, t)$ using the geostrophic velocity field $\boldsymbol{v}(\boldsymbol{x}, t)$, that we denote by $Ah = \boldsymbol{v} \cdot \nabla h$ and $Dh = \partial_t h + Ah$, respectively; processing details can be found in Appendix B. If the singularity exponents delineate streamlines, then the advective derivative should be zero, $Ah = 0$. If the singularity exponents are passive tracers, then the material derivative equals zero, $Dh = 0$. In Figs. 3 and 4, we show examples of the computation of both types of derivative in two different months of the year 2003; notice that in the figures we show the time average for the considered period of the absolute values of the time derivative. For comparison purposes, we present the derivatives of both SST and singularity exponents.

As shown in the figures, both time derivatives are close to zero in the case of singu-

OSD
6, 129–151, 2009

larity exponents, although advective derivatives are significantly smaller. This means that the hypothesis that singularity exponents delineate streamlines is more consistent than the hypothesis of passive advection of singularity exponents. However, the partial time derivative of the singularity exponents, i.e. the term $\partial_t h$, is relatively small and so both types of derivative are not so different; hence, the hypothesis of passive advection of singularity exponents can be appropriate for short time periods. Comparing the results of the time derivatives of singularity exponents and those of SST is not straightforward, as they do not have the same units. Time derivatives of SST seem to be much less uniform than those of singularity exponents and significantly greater in value, but lacking of an appropriate conversion unit the used colorbars are conventional and so this conclusion is rather arbitrary. In fact, average advective derivatives of SST are of about 0.5°C/day, which do not seem very large. To help comparison, we have defined new quantities with the same dimensions for both variables and informative about the quality as fluid tracers of each variable. We thus define the advective divergence speed, V_A, and the material divergence speed, V_M, of a scalar θ as follows:

$$V_A(\boldsymbol{x},t) \equiv \frac{|A\theta(\boldsymbol{x},t)|}{|\nabla\theta(\boldsymbol{x},t)|} \quad , \quad V_M(\boldsymbol{x},t) \equiv \frac{|D\theta(\boldsymbol{x},t)|}{|\nabla\theta(\boldsymbol{x},t)|} \tag{3}$$

These quantities have units of speed, and we interpret them as the speeds at which the isolines of θ separate from the actual streamlines. This interpretation is supported by the implicit function identity $\partial_t\theta/\partial_x\theta = -\partial_t x$. A more precise argument in support of this interpretation is the following: the advective (vs. material) time derivative informs us about the rate of variation of the variable θ as we move along the streamline (vs. trajectory), but gives no idea about the distance that the water parcel has run to observe such an increment of the variable. On the other hand, the gradient of θ gives information about the spatial variability of θ going along the direction of fastest variation, which is always perpendicular to the isolines of θ. Hence, the ratio of the time derivative by the gradient gives us the speed at which the streamline (vs. trajectory) crosses isolines of θ.

OSD
6, 129–151, 2009

We show examples of divergence speeds in Figs. 5 and 6. Figures show that both advective and material divergence speeds of singularity exponents have small values, which are of the order 1–2 km/day on average. In addition, divergence speeds are very uniformly distributed on the Globe, with more significant deviations on areas of larger mesoscale activity around the great boundary currents.

The situation is quite different for SST-derived divergence speeds. Advective divergence speeds are relative small on average (around 8 km/day) but less uniformly distributed that their singularity counterparts. Material divergence speeds, on the other hand, have rather large values, of order 30 km/day on average, with peaks up to 50 km/day, and are more associated to some frontal areas and possibly to the presence of active upwelling/downwelling, which indeed changes the thermal signature on the affected areas.

5 Conclusions

We have shown that singularity analysis of MW SST images can be used to uncover the circulation patterns in global oceans. Singularity exponents are dimensionless quantities, and they are less affected by large-area effects like sun heating cycles, sunglint, etc. In addition, they have much richer spatial structure, with strong variations, what aids to give a precise location to mesoscale features like eddies and filaments. Results indicate that singularity exponents are appropriate to delineate instantaneous streamlines with an average uncertainty of about 1 km/day, that is, around 1 cm/s. This value of the divergence speed is the smallest possible one, as it is of the order of altimeter accuracy. This result means a significant improvement with respect to other techniques employed to extract dynamic information on SST such as MCC (Bowen et al., 2002) or Surface Quasi Geostrophy (Isern-Fontanet et al., 2006). However, singularity analysis does not provide access to the full velocity vector, just to its direction. The modulus and sense of this field can be guessed under the appropriate hypothesis (Turiel et al., 2005b) or integrating additional information (Isern-Fontanet et al., 2007). In this sense

OSD
6, 129–151, 2009

the combination with the information of the forthcoming generation of wide-swath altimeters (Chelton, 2001) will mitigate such a limitation providing an improvement of the results.

As MW SST images are now produced at a daily rate, the techniques described in this paper are relevant for many purposes. At a operational level it can eventually produce high resolution operational instantaneous velocity fields. At a more fundamental level it enables a better use of the satellite information to study many oceanographic processes. We can easily determine the position of different fronts associated to the Antarctic Circumpolar Current, to quantify the extent and propagation speed of Tropical Instability Waves or to study the filamentation of the great boundary currents and how they close the great subtropical gyres at the eastern boundary. All those structures are strongly linked to large-extent phenomena which condition the climate; the re-analysis of existing databases and the on-going produced maps will be useful to understand the short-term variability of oceanic part of the climate engine and to improve our knowledge in future years.

Appendix A

Application of singularity analysis

For the determination of the singularity exponents we have employed as wavelet Ψ an optimized numerical implementation of the Lagrangian wavelet,

$$\Psi_L(\boldsymbol{x}) = \frac{1}{1 + |\boldsymbol{x}|^2} \tag{A1}$$

Such a function is not an admissible wavelet (Daubechies, 1992) because it is strictly positive and hence it cannot be used to represent data. However, as discussed in (Turiel et al., 2006), positive wavelets can be used to obtain the singularity exponents of multifractal measures as the ones defined by gradient modulus, so Ψ_L can be used

to this purpose. In fact, it has been shown to have a good performance on real situations, although it truncates the singularities beyond h=0. To avoid this effect, which is connected with the behavior of the tail of the wavelet (Turiel et al., 2008b), we have constructed a numerical implementation, Ψ_{Ln}, which is defined by a matrix of numerical weights which is close to Ψ_L for small values of $|\boldsymbol{x}|$ but has a faster decay for larger values of $|\boldsymbol{x}|$.

The exponents $h(\boldsymbol{x}, t)$ are obtained by the application of Eq. (2) at different resolution scales r. For a set of scales $r_1, r_2, \ldots, r_m$ a linear regression of $\log T_\Psi[\nabla\theta](\boldsymbol{x}, r)$ vs. $\log r$ is performed at each point $\boldsymbol{x}$ in the image; the slope of such a regression is the singularity exponent $h(\boldsymbol{x})$. For the experiences shown in this paper we have used m=7 different scales which are uniformly sampled in a logarithmic axis, $\log r_{i+1} - \log r_i$=constant. We fix the constant so that r_1=1 pixel and r_m=0.1×image size.

Appendix B

Evaluation of time derivatives

For the determination of the advective and material derivatives of the different scalars we need to compute the Lagrangian trajectories, for which we have used a simple integration scheme. Let us first introduce some notation. We will denote the longitude coordinate by ϕ and the latitude coordinate by λ. For two points on the sphere $\boldsymbol{p}=(\phi, \lambda)$, $\boldsymbol{p}'=(\phi', \lambda')$ we define the distance between them by the length of arc of geodesic circle which joints both points. For two points of close coordinates we approximate this distance $d(\boldsymbol{p}, \boldsymbol{p}')$ by the following expression:

$$d(\boldsymbol{p}, \boldsymbol{p}') = R_e \sqrt{(\lambda - \lambda')^2 + (\phi - \phi')^2 \cos^2\left(\frac{\lambda + \lambda'}{2}\right)} \tag{B1}$$

where R_e is the radius of Earth and the angular variables are expressed in radians.

OSD
6, 129–151, 2009

Given a point $\boldsymbol{p}$ in the sphere, we evaluate the velocity at that point by interpolating the velocities of the four closest points. If the four first neighbors of $\boldsymbol{p}$ on the velocity grid are the points $\boldsymbol{q}_1$, $\boldsymbol{q}_2$, $\boldsymbol{q}_3$ and $\boldsymbol{q}_4$, we evaluate the velocity at $\boldsymbol{p}$ as follows:

$$\boldsymbol{v}(\boldsymbol{p}, t) = \sum_{i \text{ valid}} \frac{Z}{d(\boldsymbol{p}, \boldsymbol{q}_i)} \boldsymbol{v}(\boldsymbol{q}_i, t) \tag{B2}$$

where the sum in the expression above is restricted to valid points (i.e. points on the ocean with measured velocity) and the normalization constant Z is such that all the weights sum up to 1,

$$Z^{-1} = \sum_{i \text{ valid}} \frac{1}{d(\boldsymbol{p}, \boldsymbol{q}_i)} \tag{B3}$$

When none of the four first neighbor points has a valid velocity we consider the point $\boldsymbol{p}$ cannot be assigned a valid velocity.

A trajectory $\boldsymbol{p}(t)$ is constructed by integrating velocity maps, interpolated in both space and time, with one-hour time increments, that is:

$$\boldsymbol{p}(t + \Delta t) = \boldsymbol{p}(t) + \boldsymbol{v}(\boldsymbol{p}(t), t)\Delta t \tag{B4}$$

where here Δt=1 h.

To compute the advective and material derivatives of a scalar $\theta(\boldsymbol{x}, t)$ we need to compute its increments along a trajectory for constant and time-varying maps, respectively. We evaluate the value of the scalar θ at a non-grid point $\boldsymbol{p}$ in a similar way to what is done with the velocity, namely:

$$\theta(\boldsymbol{p}, t) = \sum_{i \text{ valid}} \frac{Z}{d(\boldsymbol{p}, \boldsymbol{q}_i)} \theta(\boldsymbol{q}_i, t) \tag{B5}$$

OSD
6, 129–151, 2009

The interpolation on singularity exponents should be treated in a slightly different way, however. When considering singularity exponents $h(\boldsymbol{x}, t)$ it should be taken into account that variables $h(\boldsymbol{x}, t)$ are not additive and hence they cannot be linearly interpolated. According to Eq. (2), what is additive is $r^{h(\boldsymbol{x},t)}$, so we should hence interpolate $h(\boldsymbol{p}, t)$ according to the following expression:

$$r^{h(\boldsymbol{p},t)} = \sum_{i \text{ valid}} \frac{Z}{d(\boldsymbol{p}, \boldsymbol{q}_i)} r^{h(\boldsymbol{q}_i,t)} \tag{B6}$$

where r is the resolution scale at which singularity exponents are calculated. The value of r can be difficult to obtain in real situations, but we can take advantage of the fact it is very small in our case, so we can simplify the expression above by considering the dominant term,

$$h(\boldsymbol{p}, t) = \min_{i \text{ valid}} \{h(\boldsymbol{q}_i, t)\} \tag{B7}$$

that is, the exponent at the point $\boldsymbol{p}$ is the minimum of the exponents of the valid neighboring points.

The advective derivative of θ at the point $\boldsymbol{p}(t)$ and time t is given by the variation of θ along the trajectory for a constant map and time increment Δt=1 day, according the equation:

$$A\theta(\boldsymbol{p}(t), t) = \frac{\theta(\boldsymbol{p}(t + \Delta t), t) - \theta(\boldsymbol{p}(t), t)}{\Delta t} \tag{B8}$$

while the material derivative is evaluated taking into account that the map θ itself evolves,

$$D\theta(\boldsymbol{p}(t), t) = \frac{\theta(\boldsymbol{p}(t + \Delta t), t + \Delta t) - \theta(\boldsymbol{p}(t), t)}{\Delta t} \tag{B9}$$

In Figs. 3 and 4, we show the time averages of the absolute values of these derivatives, denoted by $\bar{A\theta}(\boldsymbol{x}, t)$ and $\bar{D\theta}(\boldsymbol{x}, t)$. In the case of the time-averaged advective derivative,

OSD
6, 129–151, 2009

at each time t we take each point in the ocean as the origin and we integrate for a single time step Δt; the advective derivatives at the same point and different times are averaged together. In the case of the time-averaged material derivative, we take each point on the ocean grid as starting point of the respective trajectory, that we follow for all the days in the time period used to average, then the material derivatives starting from the same point at the initial day are averaged together.

To avoid divergences due to cancellations in the gradient in Eq. (3), both the time derivative and the gradient are weighted with a fast-decreasing kernel, namely $(1+|\boldsymbol{r}|^2)^{-1}$.

Acknowledgements. This is a contribution to the EU MERSEA project (AIP3-CT-2003-502885) and to the Spanish projects OCEANTECH (PIF 2006 project) and MIDAS-4 (ESP2005-06823-C05-1).

References

Arneodo, A., Argoul, F., Bacry, E., Elezgaray, J., and Muzy, J. F.: Ondelettes, multifractales et turbulence, Diderot Editeur, Paris, France, 169 pp., 1995. 134

Bowen, M., Emery, W., Wilkin, J., Tildesley, P., Barton, I., and Knewtson, R.: Extracting multi-year surface currents from sequential thermal imagery using the Maximum Cross-correlation Technique, J. Atmos. Oceanic Technol., 19, 1665–1676, 2002. 131, 138

Chapron, B., Collard, F., and Ardhuin, F.: Direct measurement of ocean surface velocity from space: Interpretation and validation, J. Geophys. Res., 110, C0022, doi:10.1029/2004JC0022, 2005. 130

Chelton, D. B.: Report of the High-Resolution Ocean Topography, Tech. rep., Science Working Group Meeting Report, http://www.coas.oregonstate.edu/research/po/research/hotswg/, 2001. 139

Crocker, R., Emery, W., Matthews, D., and Baldwin, D.: Computing Ocean Surface Currents from Infrared and Ocean Color Imagery, IEEE Trans. Geosci. Rem. Sens., 45, 435–447, 2007. 131

Daubechies, I.: Ten lectures on wavelets, CBMS-NSF Series in App. Math., Capital City Press, Montpelier, Vermont, 1992. 131, 134, 139

Frisch, U.: Turbulence, Cambridge Univ. Press, Cambridge MA, 312 pp., 1995. 135
Isern-Fontanet, J., Chapron, B., Lapeyre, G., and Klein, P.: Potential use of microwave sea surface temperatures for the estimation of ocean currents, Geophys. Res. Lett., 22, L24608, doi:10.1029/2006GL027801, 2006. 138
Isern-Fontanet, J., Turiel, A., Garcia-Ladona, E., and Font, J.: Microcanonical Multifractal Formalism: application to the estimation of ocean surface velocities, J. Geophys. Res., 112, C05024, doi:10.1029/2006JC003878, 2007. 132, 134, 138
Johannessen, J., Kudryavtsev, V., Akimov, D., Eldevik, T., Winther, N., Johannessen, O., and Chapron, B.: On Radar Imaging of Current Features; Part 2: Mesoscale Eddy and Current Front detection, J. Geophys. Res., 110, C07017, doi:10.1029/2004JC002802, 2005. 130
Kraichnan, R.: Small-scale structure of a scalar field convected by turbulence, Phys. Fluids, 11, 945–963, 1968. 131
Lagerloef, G., Mitchum, G. T., Lukas, R. B., and Niiler, P. P.: Tropical pacific near surface currents estimated from altimeter, winds and drifter data, J. Geophys. Res., 104, 23313–23326, 1999. 134
Lapeyre, G., Hua, B., and Klein, P.: Dynamics of the orientation of active and passive scalars in two dimensional turbulence, Phys. Fluids, 13, 251–264, 2001. 131
Larnicol, G., Guinehut, S., Rio, M.-H., Drevillon, M., Faugere, Y., and Nicolas, G.: The global observed ocean products of the French Mercator project, in: Proceedings of the "15 years of progress in Radar altimetry" ESA Symposium, ESA, Venice, 2006. 133
Mallat, S.: A Wavelet Tour of Signal Processing, Academic Press, 2nd Edition, 577 pp., 1999. 134
Nieves, V., Llebot, C., Turiel, A., Solé, J., García-Ladona, E., Estrada, M., and Blasco, D.: Common turbulent signature in sea surface temperature and chlorophyll maps, Geophys. Res. Lett., 34, L23602, doi:10.1029/2007GL030823, 2007. 132, 134
Pascual, A., Faugere, Y., Larnicol, G., and Traon, P. L.: Improved description of the ocean mesoscale variability by combining four satellite altimeters, Geophys. Res. Lett, 33, 611, doi:10.1029/2005GL024633, 2006. 131, 133, 136
Reynolds, R. and Smith, T.: Improved global sea surface temperature analyses using optimal interpolation, J. Climate, 7, 929–948, 1994. 133
Rio, M.-H., Schaeffer, P., Lemoine, J.-M., and Hernandez, F.: The estimation of the ocean Mean Dynamic Topography through the combination of altimetric data, in-situ measurements and GRACE geoid: From global to regional studies, in: Proceedings of GOCINA, Luxembourg,

2005. 133
Traon, P. L. and Dibarboure, G.: An illustration of the unique contribution of the TOPEX/Poseidon – Jason-1 tandem mission to mesoscale variability studies, Marine Geodesy, 27, 3–13, 2004. 133
Traon, P. L., Nadal, F., and Ducet, N.: An improved mapping method of multisatellite altimeter data, J. Atmos. Oceanic Technol., 15, 522–534, 1998. 131
Traon, P. L., Faugère, Y., Hernandez, F., Dorandeuand, J., Mertz, F., and Ablain, M.: Can we merge GEOSAT Follow-On with TOPEX/POSEIDON and ERS-2 for an improved description of the ocean circulation?, J. Atmos. Oceanic Technol., 20, 889–895, 2003. 133
Turiel, A. and Parga, N.: The multi-fractal structure of contrast changes in natural images: from sharp edges to textures, Neural Computation, 12, 763–793, 2000. 131, 134
Turiel, A., Grazzini, J., and Yahia, H.: Multiscale techniques for the detection of precipitation using thermal IR satellite images, IEEE Geosci. Remote Sens. Lett., 2, 447–450, doi:10.1109/LGRS.2005.852712, 2005a. 134
Turiel, A., Isern-Fontanet, J., García-Ladona, E., and Font, J.: Multifractal method for the instantaneous evaluation of the stream function in geophysical flows, Phys. Rev. Lett., 95, 104502, doi:10.1103/PhysRevLett.95.104502, 2005b. 132, 134, 138
Turiel, A., Pérez-Vicente, C., and Grazzini, J.: Numerical methods for the estimation of multifractal singularity spectra on sampled data: a comparative study, J. Computat. Phys., 216, 362–390, 2006. 139
Turiel, A., Solé, J., Nieves, V., Ballabrera-Poy, J., and García-Ladona, E.: Tracking oceanic currents by singularity analysis of Micro-Wave Sea Surface Temperature images, Rem. Sens. Environ., 112, 2246–2260, 2008a. 132, 134
Turiel, A., Yahia, H., and Pérez-Vicente, C.: Microcanonical Multifractal Formalism: a geometrical approach to multifractal systems. Part I: Singularity analysis, J. Phys. A, 41, 015 501, doi:10.1088/1751-8113/41/1/015501, 2008b. 135, 140
Wunsch, C. and Stammer, D.: Satellite altimetry, the marine geoid, and the oceanic general circulation, Ann. Rev. Earth Planet. Sci., 26, 219–353, 1998. 131

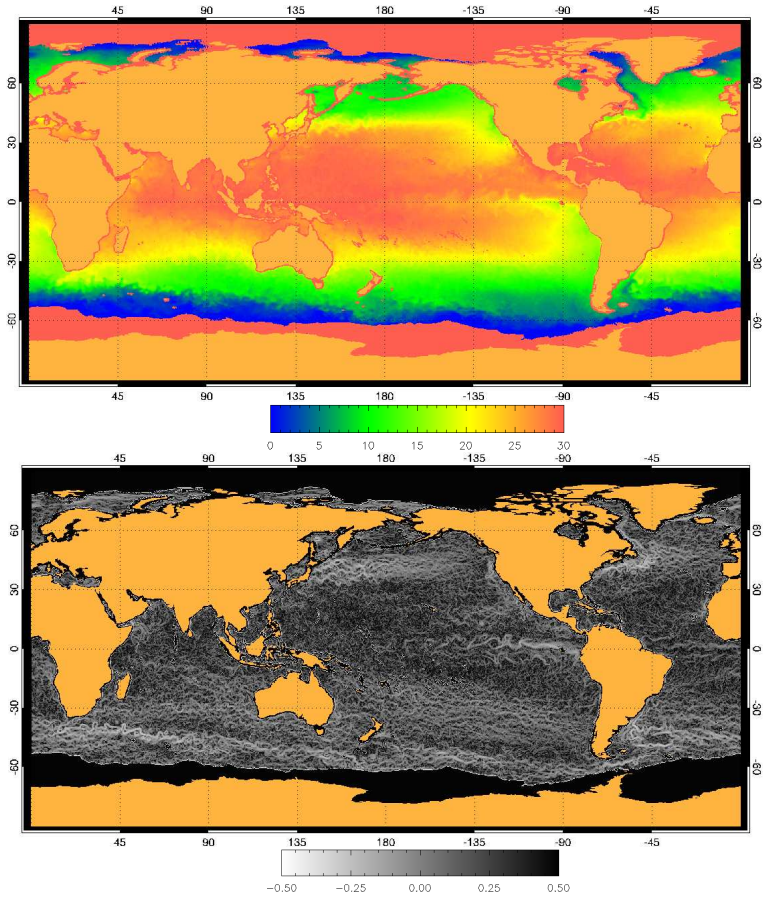

Fig. 1. Top: Global MW SST image for 1 October 2005; units in color bar are Celsius degrees. Bottom: Associated map of singularity exponents (which have no units).

OSD

6, 129–151, 2009

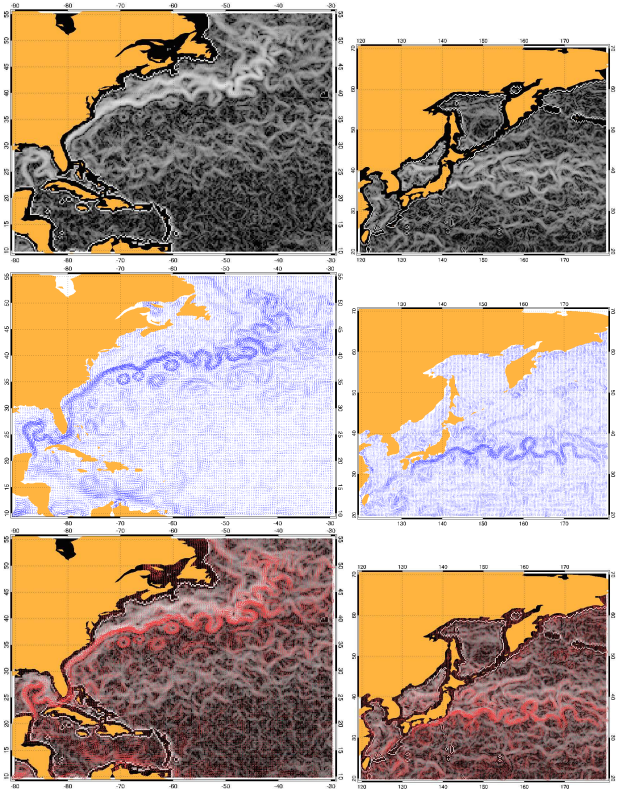

Fig. 2. From top to bottom: Singularity exponents derived from MW SST for two different areas and times; altimeter-derived geostrophic velocities for the same locations and times; and superimposition of both fields. The colorbar for the singularity exponent maps is the same as in Fig. 1; the maximum length of velocity vectors corresponds to 1 m/s. Results on the left column are for Gulf Stream area on 1 February 2003; results on the right are for Kuroshio current on 1 November 2002.

OSD

6, 129–151, 2009

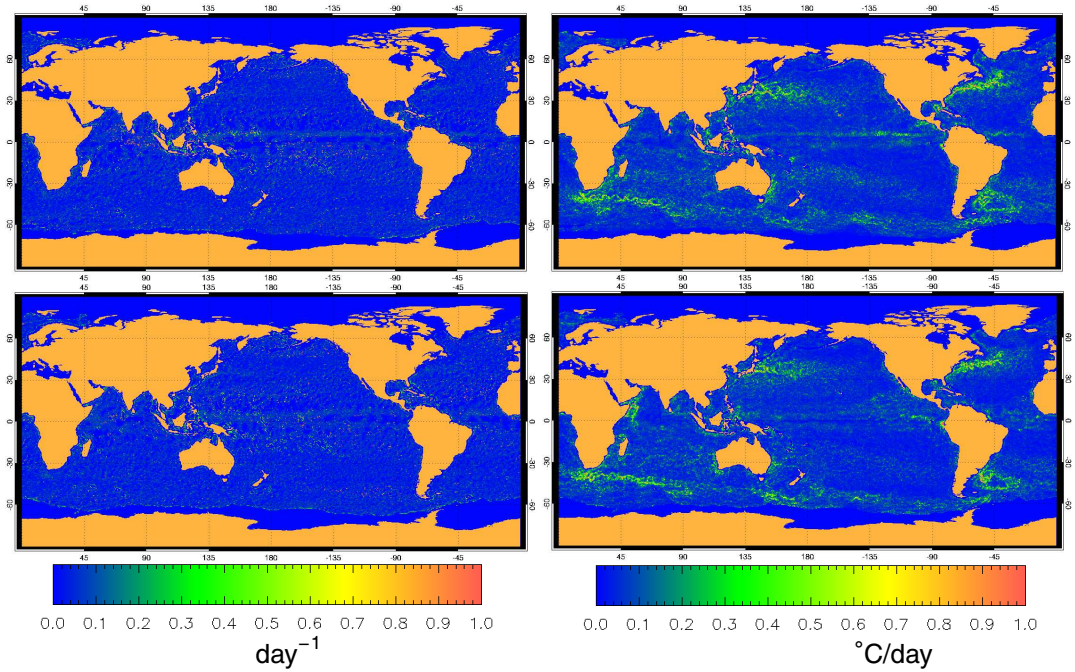

Fig. 3. Time averages of the absolute value of advective derivatives of singularity exponent maps (left) and SST (right), for a period of three consecutive days. Results on the top row correspond to the period 1–3 January 2003; results on the bottom row are for 1–3 July 2003. The spatial averages of these quantities are as follows: Singularity exponents: 0.065 day^{-1} (January) and 0.068 day^{-1} (July); SST: 0.53°C/day (January) and 0.51°C/day (July).

OSD
6, 129–151, 2009

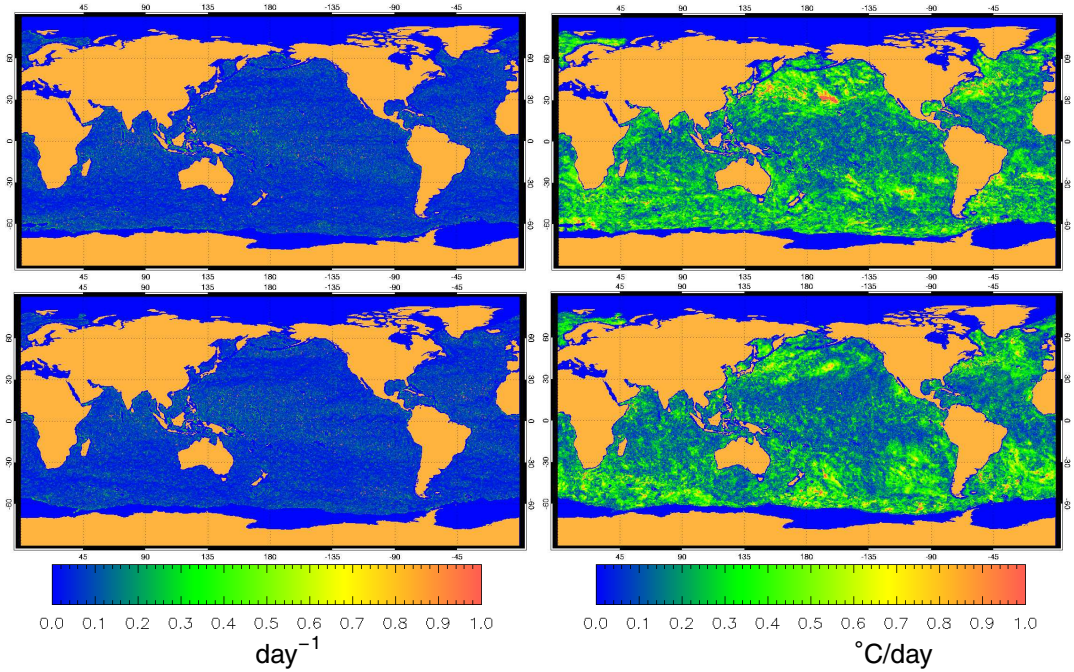

Fig. 4. Time averages of absolute values of material derivatives of singularity exponent maps (left) and SST (right) for a period of three consecutive days. Results on the top row correspond to the period 1–3 January 2003; results on the bottom row are for 1–3 July 2003. The spatial averages of these quantities are as follows: Singularity exponents: 0.11 day^{-1} (January) and 0.11 day^{-1} (July); SST: 1.65°C/day (January) and 1.49°C/day (July).

OSD
6, 129–151, 2009

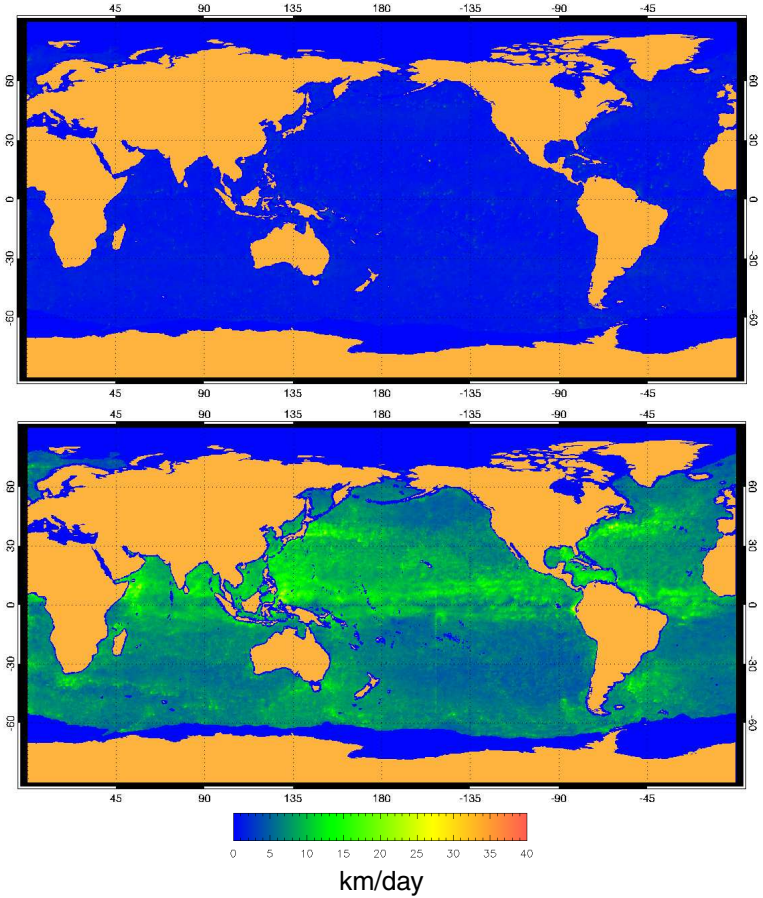

Fig. 5. Advective divergence speed maps obtained from singularity exponents (top) and from SST (bottom); results are for the time average over the days 1 to 3 July 2003. The spatially averaged advective divergence speeds are 1.03 km/day for singularity exponents and 7.59 km/day for SST.

OSD

6, 129–151, 2009

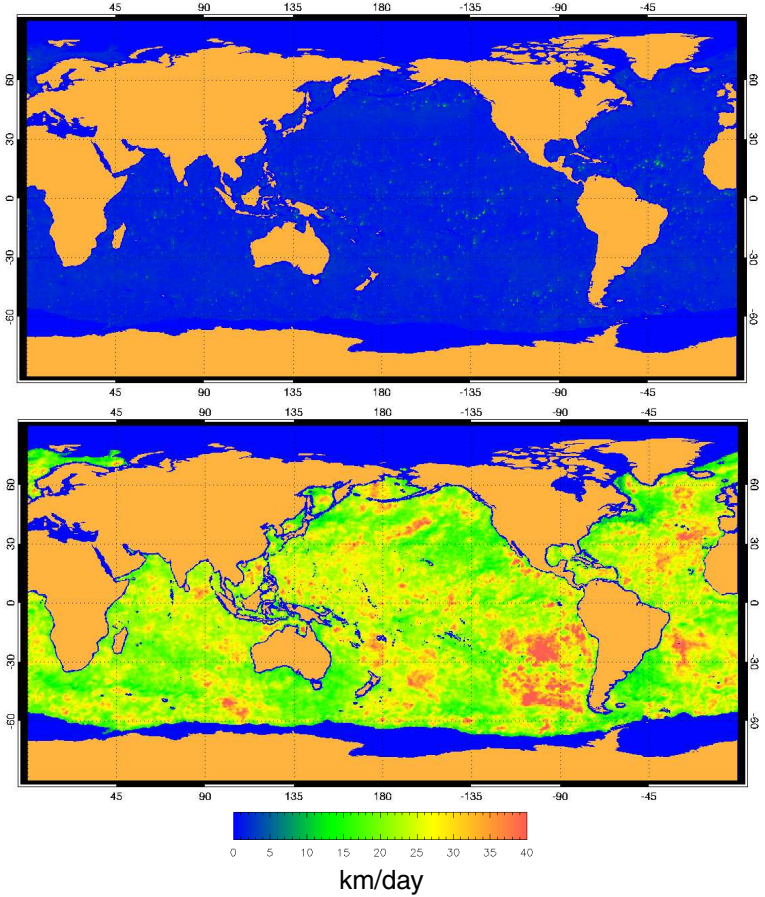

Fig. 6. Material divergence speed maps obtained from singularity exponents (top) and from SST (bottom); results are for the time average over the days 1 to 3 July 2003. The spatially averaged material divergence speeds are 1.61 km/day for singularity exponents and 23.57 km/day for SST.

OSD

6, 129–151, 2009